Environ Fluid Mech (2014) 14:235–261
DOI 10.1007/s10652-013-9308-1

ORIGINAL ARTICLE

Waves of intermediate length through an array of vertical cylinders

Chiang C. Mei · I.-Chi Chan · Philip L.-F. Liu

Received: 31 May 2013 / Accepted: 21 August 2013 / Published online: 27 September 2013

Abstract We report a semi-analytical theory of wave propagation through a vegetated water. Our aim is to construct a mathematical model for waves propagating through a lattice-like array of vertical cylinders, where the macro-scale variation of waves is derived from the dynamics in the micro-scale cells. Assuming infinitesimal waves, periodic lattice configuration, and strong contrast between the lattice spacing and the typical wavelength, the perturbation theory of homogenization (multiple scales) is used to derive the effective equations governing the macro-scale wave dynamics. The constitutive coefficients are computed from the solution of micro-scale boundary-value problem for a finite number of unit cells. Eddy viscosity in a unit cell is determined by balancing the time-averaged rate of dissipation and the rate of work done by wave force on the forest at a finite number of macro stations. While the spirit is similar to RANS scheme, less computational effort is needed. Using one fitting parameter, the theory is used to simulate three existing experiments with encouraging results. Limitations of the present theory are also pointed out.

Keywords Water Waves · Vegetated Waters · Coastal dynamics · Tsunami Protection · Theory of multiple scales · Theory of homogenization · Eddy Viscosity model

1 Introduction

The fluid dynamics of wind and river current in the presence of plants or grass has been the subject of extensive studies for a long time. Vast literature exists on field and laboratory

C. C. Mei (✉)
Department of Civil and Environmental Engineering, Massachusetts Institute of Technology, Cambridge, MA, USA
e-mail: CCMEI@MIT.EDU

I.-C. Chan, P. L.-F. Liu
School of Civil and Environmental Engineering, Cornell University, Ithaca, NY, USA

P. L.-F. Liu
Institute of Hydrological and Oceanic Sciences, National Central University, Jungli, Taiwan

observations as well as mathematical modeling of wind over a forest [27], river or lake flow over canopy [26], or tides through coastal mangroves [18], etc. Vegetation of course affects the direction and pattern of fluid flow. In turn the flow exerts forces on the plant branches and alters the diffusion and convection of nutrients and chemicals, thereby affects the growth and survival of plants and of the marine life around them. Because of its influence on coastal inundation, beach erosion and the ecological health of coastal waters, the interaction of vegetation and storm waves or tsunamis have also received increasing attention. For example, wave flume simulation of kelps, seagrasses, and coastal trees have been conducted by [1,3,6,7,23,29,33,34,38,40,42], among others. Mathematical models starting from *macro-scale (wavelength-scale)* equations have been proposed by many (e.g., [5,16,22,17] etc.). Typically the inviscid and irrotational theory is used as the basis. Drag and inertia forces via Morison's formula are added in an *ad hoc* manner to account for wave attenuation. The prediction of attenuation rate depends on proper data fitting of two empirical coefficients. A depth-averaged model for waves over a canopy of vertical cylinders with height less than the sea depth has been reported by Lowe et al. [15]. In their model, the canopy resistance force is described by the Morison equation and the shear stress at the top of the canopy is represented by the parameterized quadratic friction. Vo-Luong and Massel [39] extended this approach further by adding another empirical term to account for breaking.

Since the presence of vegetation is the main source of turbulence, a more fundamental model needs to account for the micro-scale motion in the small space between the cylinders. Moreover, the macro-scale transport of solvents or fine particles depend on the effective diffusivity which may depend on the local flow in the interstices. Hence a theory accounting for the micro-scale variations is needed. For a steady, uniform current passing through a cylinder array, Stoesser et al. [32] have applied the numerical method of large eddy simulation (LES) to model a current through a periodic array of many cylinders in an open channel, and compared with laboratory measurements of Liu et al. [14]. Mo [24] developed a large eddy sub-grid model to investigate a non-breaking non-periodic solitary wave interacting with slender vertical piles. By employing Smagorinsky's [30] model to relate the eddy viscosity to the local dissipation rate on the sub-grid level, the free-surface profiles, simulated by the volume of fluid (VOF) method, agree well with the laboratory data. However, the comparison on the dynamic pressure is not as good. For periodic waves through vegetation involving many vertical cylinders, Li and Yan [13] have developed a numerical model based on the Reynolds-averaged Navier–Stokes equations (RANS). The eddy viscosity is obtained by solving a transport equation proposed by Spalart and Allmaras [31] developed for aerodynamic flows without vegetation. The presence of vegetation is accounted for by adding a source term in the transport equation and by adding Morison's force in the momentum equation. RANS technique has also been applied by Wu et al. [42] to study periodic wave transmission and reflection from an array of vertical cylinders. They employed the Smagorinsky model for sub-grid turbulence and added Morison's force with drag and inertia coefficients calibrated by the measured wave amplitudes to incorporate the vegetation effects.

Both LES and RANS methods require closure schemes at the sub-grid level, involve a number of empirical coefficients, and demand considerable computational effort for a region with many cylinders. Furthermore, except in very shallow water where breaking dominates, turbulence in waves owes its existence to vegetation. Hence the rationale of adding Morison forces to a turbulence model established for non-vegetated flows appears to be double counting. Direct superposition of the two amounts to assuming turbulence already exists even in the absence of vegetation; this is rarely the case outside the surf zone. In order to reduce the effort of numerical computation without totally glossing over the interstitial dynamics, and to facilitate physical insight, the present authors have made use of the sharp

contrast between wavelength and plant spacing, and applied the perturbation techniques of multiple scales *(homogenization)* [21]. By this technique the macro-scale physics of wave propagation is found to resemble a transient flow through a porous medium. Unlike the classical approach in groundwater hydraulics, here the dynamic Darcy's law and permeability are derived from the solution of a micro-scale problem in a unit cell. A special feature of this approach is that heavy numerical effort is focused only around one or a few cylinders in a small cell without involving all cylinders at once. Wave motion on the macro scale is predicted from cell-averaged equations, which can be solved either analytically or by less cumbersome numerical schemes.

The homogenization method is most effective for linear problems. To conform with this restriction the wave amplitude must be small. Although more sophisticated models are in principle possible, we shall assume for simplicity that the eddy viscosity is constant in a unit cell. In an earlier study of steady current through vegetation, an eddy viscosity was introduced by order of magnitudes estimates of the cell-averaged dissipation and the work done by the measured drag force on the entire array [26]. In principle, this eddy viscosity is related nonlinearly to the local flow, hence its use in a linearized wave theory amounts to quasi-linearization similar to the approximation of the quadratic wave drag on offshore piles by a term linear in velocity [28]. Inspired by the evidence of damping of tsunami by mangroves, Mei et al. [21] used this steady-state relation on long-period waves in shallow water through a periodic array of many vertical cylinders, spaced at small distances comparable to depth. By solving the macro-scale equations derived from the solution of a typical unit cell, predictions on wave amplitudes are found to be in good agreement with data from wave flume measurements.

In many coastal environments, vegetation often exists in water depth comparable to the wavelength. For sustained waves of relatively short period we are only aware of the articles by Augustin [2], Huang and Zhang [11], and Wu et al. [42]. Limited experimental data for non-periodic tsunamis through a Green Belt have been reported by Hiraishi and Harada [9], Harada and Imamura [8], and Huang et al. [10]. In this article we extend the mathematical model of Mei et al. [21] to waves of intermediate period and length. The unit cell has horizontal dimensions much smaller than the height, hence the micro-scale problem is now three dimensional. New macro-scale equations are derived with constitutive coefficients calculated from the solution of the cell problems. A key point of this study is to compute the eddy viscosity by making use of the drag force information from experiments. Since extensive data for a large array of cylinders exist only for steady forces induced by a uniform current [4], a time-independent eddy viscosity is found by combining an energy argument with the drag force measured in steady flows. This eddy viscosity is then used for micro-scale computations. As the eddy viscosity depends on the local averaged flow which varies on the macro scale, the micro and macro problems are solved by sequential iteration. With just one fitting coefficient, predictions of wave characteristics are in encouraging agreement with available wave measurements from several experiments. It is hoped that comprehensive data will become available in the future for wave forces on cylinder arrays, so that empirical information can be employed with greater confidence to give a micro-scale-based but a computationally expedient model for predicting the interaction of waves and vegetation.

2 Formulation for infinitesimal waves

Let $\vec{x} = (x_1, x_2)$ and z denote the horizontal and vertical Cartesian coordinates respectively with origin at the mean sea level. For simplicity we consider a sea of finite and constant depth,

h_0. The vegetation is idealized by a periodic array of vertical rigid cylinders taller than the sea depth, and are fixed over a large area of the seabed. Infinitesimal waves of characteristic frequency ω and amplitude a_0 enter the emergent vegetation from the open sea. The scale of the wavelength is $1/k_0$ where $k_0 \equiv \omega^2/g$ is the characteristic wavenumber with g being the gravitational acceleration. We assume that the sea depth is comparable to the wavelength, i.e., $k_0 h_0 = \mathcal{O}(1)$, but much greater than the cylinder spacing ℓ, i.e., $k_0 \ell \ll 1$. Throughout this article $1/k_0$ and h_0 are regarded as the macro-scale lengths, and ℓ and the cylinder diameter, $\mathcal{D}$, as the micro scales.

Let u_i and w be the horizontal and vertical velocity components. Continuity requires that

$$\frac{\partial u_i}{\partial x_i} + \frac{\partial w}{\partial z} = 0, \quad i = 1, 2. \tag{2.1}$$

Ignoring convective inertia for infinitesimal waves, the linearized Reynolds equations read:

$$\frac{\partial u_i}{\partial t} = -\frac{1}{\rho}\frac{\partial p}{\partial x_i} + \nu_e \left(\frac{\partial^2 u_i}{\partial x_j \partial x_j} + \frac{\partial^2 u_i}{\partial z^2} \right), \quad i, j = 1, 2, \tag{2.2}$$

and

$$\frac{\partial w}{\partial t} = -\frac{1}{\rho}\frac{\partial p}{\partial z} + \nu_e \left(\frac{\partial^2 w}{\partial x_j \partial x_j} + \frac{\partial^2 w}{\partial z^2} \right), \quad j = 1, 2, \tag{2.3}$$

where ρ is the constant fluid density, p denotes the dynamic pressure related to the the total pressure P by

$$P = p - \rho g z. \tag{2.4}$$

As stated in the introduction we shall choose a model where the eddy viscosity, ν_e, is a constant within each cell obtained by using the averaged horizontal velocity solved from the macro-scale problem at the previous iteration. The updated eddy viscosity is then used to solve the micro-scale cell problem again to provide the constitutive coefficients of the macro-scale problem for the next iteration. Details of this eddy viscosity model and the iteration procedure will be discussed later in §7.2.

On the sea bed, the no-slip condition is imposed,

$$u_i = w = 0, \quad z = -h_0. \tag{2.5}$$

On the free surface, the kinematic boundary condition requires

$$\frac{\partial \zeta}{\partial t} = w, \quad z = 0, \tag{2.6}$$

where ζ denotes the free-surface displacement. For the dynamic conditions, we require that both the normal and tangential stresses vanish,

$$g\zeta - \frac{p}{\rho} + 2\nu_e \frac{\partial w}{\partial z} = 0, \quad z = 0, \tag{2.7}$$

and

$$\frac{\partial u_i}{\partial z} + \frac{\partial w}{\partial x_i} = 0, \quad z = 0. \tag{2.8}$$

On the surface of the rigid cylinder S_B, there is no slip,

$$u_i = w = 0, \quad x_i, z \in S_B. \tag{2.9}$$

Let the following normalization be introduced:

$$x_i^* = x_i/\ell, \quad Z^* = k_0 z, \quad t^* = \omega t, \quad h^* = k_0 h,$$
$$p^* = p/(\rho g a_0), \quad u_i^* = u_i/(\omega a_0), \quad w^* = w/(\omega a_0), \quad \zeta^* = \zeta/a_0.$$

In particular the horizontal coordinates are scaled by the micro length ℓ, but the vertical coordinate by the macro length $1/k_0$.

The normalized continuity equation reads

$$\frac{\partial u_i^*}{\partial x_i^*} + \epsilon \frac{\partial w^*}{\partial Z^*} = 0, \tag{2.10}$$

where

$$\epsilon \equiv \frac{\omega^2 \ell}{g} = k_0 \ell \ll 1 \tag{2.11}$$

is the small ratio of micro-to-macro lengths. Note that (2.11) implies that predictions for the same ϵ apply to a very dense forest if the waves are short.

Let us define

$$\sigma = \frac{\nu_e}{\omega \ell^2} \tag{2.12}$$

which is expected to be no greater than $\mathcal{O}(1)$, as turbulence is caused by the narrow spacing.

The normalized horizontal momentum equations are

$$\epsilon \frac{\partial u_i^*}{\partial t^*} = -\frac{\partial p^*}{\partial x_i^*} + \epsilon\sigma \left(\frac{\partial^2 u_i^*}{\partial x_j^* \partial x_j^*} + \epsilon^2 \frac{\partial^2 u_i^*}{\partial Z^{*2}} \right), \quad i = 1, 2. \tag{2.13}$$

The vertical momentum equation is normalized to

$$\frac{\partial w^*}{\partial t^*} = -\frac{\partial p^*}{\partial Z^*} + \sigma \left(\frac{\partial^2 w^*}{\partial x_j^* \partial x_j^*} + \epsilon^2 \frac{\partial^2 w^*}{\partial Z^{*2}} \right). \tag{2.14}$$

The no-slip condition is required on the cylinder walls,

$$u_i^* = w^* = 0, \quad x^*, Z^* \in S_B, \tag{2.15}$$

and on the sea bed,

$$u_i^* = w^* = 0, \quad Z^* = -h^*. \tag{2.16}$$

On the free surface, the kinematic boundary condition requires

$$\frac{\partial \zeta^*}{\partial t^*} = w^*, \quad Z^* = 0. \tag{2.17}$$

In the absence of wind, the normal and tangential stresses vanish

$$\zeta^* - p^* + 2\epsilon^2 \sigma \frac{\partial w^*}{\partial Z^*} = 0, \quad Z^* = 0, \tag{2.18}$$

$$\epsilon \frac{\partial u_i^*}{\partial Z^*} + \frac{\partial w^*}{\partial x_i^*} = 0, \quad Z^* = 0. \tag{2.19}$$

3 Two-scale expansions

For describing the physics over two sharply contrasting scales we employ fast and slow coordinates, x_i^* and X_i^*, in the horizontal plane where

$$X_i^* = \epsilon x_i^* = k_0 x_i, \quad i = 1, 2 \text{ only}; \quad Z^* = k_0 z. \tag{3.1}$$

From here on only dimensionless variables are used with the asterisks $(\cdot)^*$ dropped for brevity. All dimensionless unknowns are expanded by

$$\begin{aligned}(u_i, w, p, \zeta) = \left(u_i^{(0)}, w^{(0)}, p^{(0)}, \zeta^{(0)}\right) + \epsilon \left(u_i^{(1)}, w^{(1)}, p^{(1)}, \zeta^{(1)}\right) \\ + \epsilon^2 \left(u_i^{(2)}, w^{(2)}, p^{(2)}, \zeta^{(2)}\right) + \cdots,\end{aligned} \tag{3.2}$$

where $u_i^{(n)}$, $w^{(n)}$, $p^{(n)}$, and $\zeta^{(n)}$ are all functions of (x_i, X_i, Z, t).

We get from continuity (2.10),

$$\frac{\partial u_i^{(0)}}{\partial x_i} + \epsilon \frac{\partial u_i^{(0)}}{\partial X_i} + \epsilon \frac{\partial u^{(1)}}{\partial x_i} + \epsilon \frac{\partial w^{(0)}}{\partial Z} = \mathcal{O}(\epsilon^2), \tag{3.3}$$

which gives the perturbation equations at orders $\mathcal{O}(1)$ and $\mathcal{O}(\epsilon)$:

$$\frac{\partial u_i^{(0)}}{\partial x_i} = 0, \tag{3.4}$$

$$\frac{\partial u_i^{(0)}}{\partial X_i} + \frac{\partial u_i^{(1)}}{\partial x_i} + \frac{\partial w^{(0)}}{\partial Z} = 0. \tag{3.5}$$

From the horizontal momentum equations (2.13), we get

$$\epsilon \frac{\partial u_i^{(0)}}{\partial t} + \epsilon^2 \frac{\partial u_i^{(1)}}{\partial t} = -\frac{\partial p^{(0)}}{\partial x_i} - \epsilon \frac{\partial p^{(0)}}{\partial X_i} - \epsilon \frac{\partial p^{(1)}}{\partial x_i} + \epsilon\sigma \frac{\partial^2 u_i^{(0)}}{\partial x_j \partial x_j} + \mathcal{O}(\epsilon^2). \tag{3.6}$$

The perturbation equations are

$$0 = -\frac{\partial p^{(0)}}{\partial x_i}, \tag{3.7}$$

$$\frac{\partial u_i^{(0)}}{\partial t} = -\frac{\partial p^{(0)}}{\partial X_i} - \frac{\partial p^{(1)}}{\partial x_i} + \sigma \frac{\partial^2 u_i^{(0)}}{\partial x_j \partial x_j}. \tag{3.8}$$

The vertical momentum equation, (2.14), gives,

$$\frac{\partial w^{(0)}}{\partial t} + \epsilon \frac{\partial w^{(1)}}{\partial t} = -\frac{\partial p^{(0)}}{\partial Z} - \epsilon \frac{\partial p^{(1)}}{\partial Z} + \sigma \frac{\partial^2 w^{(0)}}{\partial x_j \partial x_j} + \mathcal{O}(\epsilon^2). \tag{3.9}$$

Only the leading order approximation is needed, i.e.,

$$\frac{\partial w^{(0)}}{\partial t} = -\frac{\partial p^{(0)}}{\partial Z} + \sigma \frac{\partial^2 w^{(0)}}{\partial x_j \partial x_j}. \tag{3.10}$$

The kinematic boundary condition, (2.16), gives

$$u_i^{(0)} = u_i^{(1)} = w^{(0)} = w^{(1)} = 0, \quad Z = -h \tag{3.11}$$

on the seabed, while (2.17) gives

$$\frac{\partial \zeta^{(0)}}{\partial t} = w^{(0)}, \quad Z = 0 \tag{3.12}$$

on the free surface.

From (2.18), the normal stress condition on $Z = 0$ reduces to $\zeta = p + \mathcal{O}(\epsilon^2)$, hence

$$\zeta^{(0)} = p^{(0)}. \tag{3.13}$$

From (2.19), the tangential stress condition on $Z = 0$ becomes

$$\epsilon \frac{\partial u_i^{(0)}}{\partial Z} + \frac{\partial w^{(0)}}{\partial x_i} + \epsilon \frac{\partial w^{(0)}}{\partial X_i} + \epsilon \frac{\partial w^{(1)}}{\partial x_i} = \mathcal{O}(\epsilon^2), \tag{3.14}$$

which implies

$$w^{(0)}\Big|_{Z=0} = w^{(0)}(X_i, 0, t). \tag{3.15}$$

This leads to the important simplification that $\zeta^{(0)}$ and $p^{(0)}$ depend only on the macro scale of waves:

$$\zeta^{(0)} = \zeta^{(0)}(X_i, t), \quad p^{(0)} = p^{(0)}(X_i, Z, t). \tag{3.16}$$

Note however that $w^{(0)}(x_i, X_i, Z, t)$ can depend on the micro coordinate for $Z < 0$ (beneath the free surface).

On the rigid cylinders, we have

$$u_i^{(0)} = w^{(0)} = 0, \quad x_i, Z \in S_B. \tag{3.17}$$

Because of (3.16), the micro-scale variation of the leading order velocity field, $(u_i^{(0)}, w^{(0)})$, and the pressure fluctuation, $p^{(1)}$, are forced by the macro-scale gradient of $\zeta^{(0)}$ and $p^{(0)}$. Recall that by assumption ν_e is independent of time t and the fast coordinates x_i. Because the array geometry is periodic, we can consider the area of vegetation as a union of unit cells and treat the micro-scale problem in a typical cell first. By taking cell averages of the next order, the effective equation for the macro-scale motion will be derived.

From now on we limit our attention to the time-periodic case only. All unknowns will be written in the form of

$$F(x_i, X_i, Z, t) = \Re\left\{\widetilde{F}(x_i, X_i, Z)e^{-\mathrm{i}t}\right\}, \tag{3.18}$$

where $\widetilde{F}$ represents location-dependent amplitude and the operator $\Re(\cdot)$ denotes the real part. All equations in this section can be rewritten for the complex amplitudes by simply changing $\partial/\partial t$ to $-\mathrm{i}$.

4 The cell problem

Let us consider the fluid motion inside a typical cell Ω in a periodic array. The cell is bounded by the horizontal planes, $Z = -h, 0$, and by vertical side planes. One or a few solid cylinders sit inside the cell. In view of linearity, we assume the following solution for the micro-scale variation in the cell

$$\widetilde{u}_i^{(0)} = -\widetilde{K}_{ik}(\vec{x})\frac{\partial \widetilde{p}^{(0)}}{\partial X_k}, \quad \widetilde{p}^{(1)} = -\widetilde{A}_k(\vec{x})\frac{\partial \widetilde{p}^{(0)}}{\partial X_k}, \quad \widetilde{w}^{(0)} = -\widetilde{W}(\vec{x})\frac{\partial \widetilde{p}^{(0)}}{\partial Z}, \quad \vec{x} \in \Omega_f, \tag{4.1}$$

where Ω_f denotes the fluid inside Ω.

From (3.4) and (3.8), $\widetilde{K}_{ij}$ and $\widetilde{A}_j$ vary only horizontally and satisfy

$$\frac{\partial \widetilde{K}_{ik}}{\partial x_i} = 0, \quad \vec{x} \in \Omega_f, \tag{4.2}$$

$$-\mathrm{i}\widetilde{K}_{ik} = \delta_{ik} - \frac{\partial \widetilde{A}_k}{\partial x_i} + \sigma \frac{\partial^2 \widetilde{K}_{ik}}{\partial x_j \partial x_j}, \quad \vec{x} \in \Omega_f. \tag{4.3}$$

Note that the last equation can be written as

$$-\mathrm{i}\widetilde{K}_{ik} = \delta_{ik} - \frac{\partial \widetilde{A}_k}{\partial x_i} + \frac{\partial \widetilde{\tau}_{ij}^{(k)}}{\partial x_j}, \quad \vec{x} \in \Omega_f, \tag{4.4}$$

where

$$\widetilde{\tau}_{ij}^{(k)} = \sigma \left(\frac{\partial \widetilde{K}_{ik}}{\partial x_j} + \frac{\partial \widetilde{K}_{jk}}{\partial x_i} \right) \tag{4.5}$$

is the stress tensor due to forcing by unit pressure gradient in the direction k.

On the solid cylinder S_B there is no slip,

$$\widetilde{K}_{ik} = 0, \quad \vec{x}, Z \in S_B. \tag{4.6}$$

On the outer side boundaries of the cell, $\widetilde{K}_{ij}$ and $\widetilde{A}_j$ are periodic. For uniqueness, we shall impose

$$\langle \widetilde{A}_j \rangle = 0, \tag{4.7}$$

where $\langle \cdot \rangle$ defines the cell average over the horizontal cross-section,

$$\langle f \rangle = \frac{1}{\Omega} \iint_{\Omega_f} f dx_1 dx_2. \tag{4.8}$$

Projected on the horizontal plane, Ω denotes the total cross-sectional area of a unit cell. In order to ensure no slip on the sea bottom, a Stokes boundary layer of small thickness $\delta = \sqrt{2\nu_e/\omega} = \mathcal{O}(\sqrt{\sigma}\ell)$ can be fitted in principle. However, its integrated effect on the macro-scale motion is negligible, and will not be considered.

From (3.10), the vertical motion leads to the cell problem for $\widetilde{W}$:

$$-\mathrm{i}\widetilde{W} = 1 + \sigma \frac{\partial^2 \widetilde{W}}{\partial x_j \partial x_j}, \quad \vec{x} \in \Omega_f, \quad -h < Z < 0, \tag{4.9}$$

subject to the no-slip condition on S_B,

$$\widetilde{W} = 0, \quad \vec{x}, Z \in S_B, \tag{4.10}$$

and Ω-periodicity. The requirement for the vertical velocity to vanish on the seabed will be met by $\partial p^{(0)}/\partial Z = 0$.

With ν_e and σ known from the previous iteration, the horizontal and vertical cell problems above can be solved numerically by the finite element method for many stations on the macro scale only. Details are similar to that of Mei et al. [21]. For a symmetric cell geometry, as illustrated in Fig. 1, it can be shown from the cell boundary-value problems, (4.2)–(4.7), that: (i) $\widetilde{K}_{11}(x_1, x_2) = \widetilde{K}_{22}(x_2, x_1)$ and both are even in x_1 and x_2; (ii) $\widetilde{K}_{12} = \widetilde{K}_{21}$. They are also odd in x_1 and x_2 and symmetric with respect to the diagonals $x_1 - x_2 = 0$ and $x_1 + x_2 = 0$. Sample results for the micro-scale variations in a cell are shown in Fig. 2.

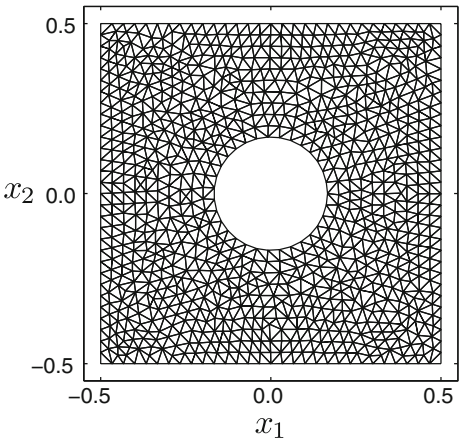

Fig. 1 Sample finite element discretization of a symmetric cell configuration: a *circular cylinder* sits at the center of a unit square cell. The cell porosity is 0.913 and 1799 *triangular* elements are used

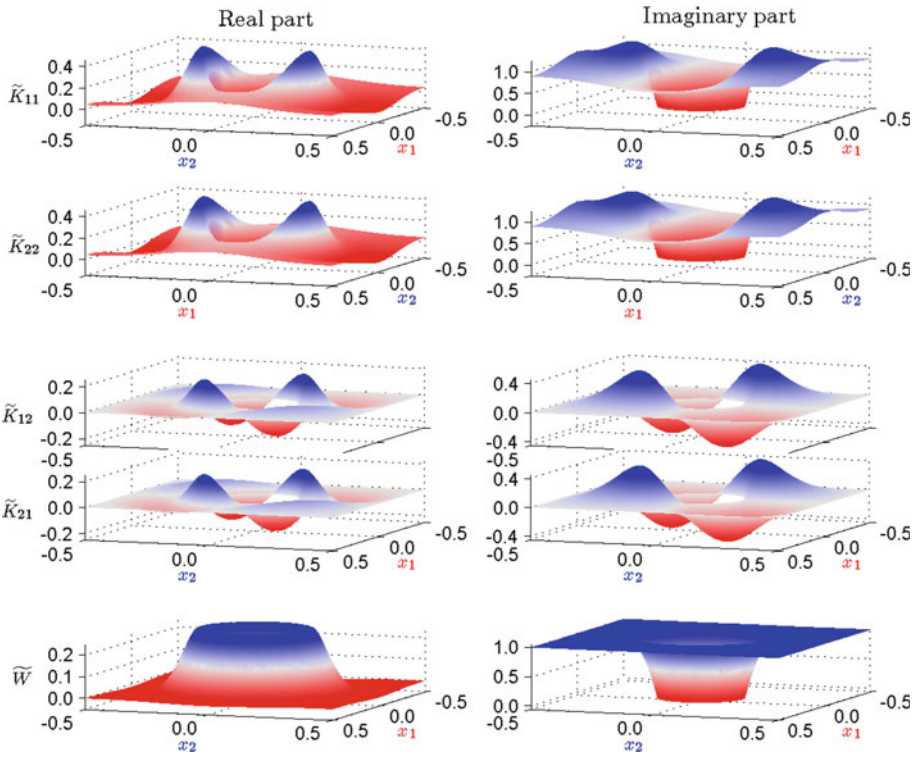

Fig. 2 Sample results for the micro-scale $\widetilde{K}_{ij}(x_1, x_2)$ and $\widetilde{W}(x_1, x_2)$. In this demonstration, $\sigma = 0.0025$ is chosen and the corresponding cell configuration is shown in Fig. 1

5 Eddy viscosity for two-dimensional waves

For the special case of steady, horizontally uniform flow through aquatic vegetation, Nepf [26] and Tanino and Nepf [36] have given the following relation between the eddy viscosity and the drag force on the entire forest:

$$\nu_e \propto \left[C_{D,\,\text{steady}} \frac{1-n}{n} \right]^{1/3} U_{mean} \mathcal{D}, \tag{5.1}$$

where U_{mean} is the averaged velocity through the vegetation,

$$n = \frac{\Omega_f}{\Omega} \tag{5.2}$$

is the cell porosity, and $C_{D,\,\text{steady}}$ is drag coefficient from laboratory experiments. This simple relation has been used by Mei et al. [21] for long-period waves through emergent vegetation. We note that (5.1) was derived by balancing the total dissipation rate and the rate of work done by the drag force on the entire forest, with some order-of-magnitude estimates.

For an isolated cylinder in an oscillatory flow of ambient velocity $U(t)$, the force is commonly calculated from Morison's formula [25]:

$$\text{Force} = \frac{\rho}{2} C_{D,\,\text{single}} U|U| \mathcal{D} + \rho C_{M,\,\text{single}} \frac{dU}{dt} \frac{\pi \mathcal{D}^2}{4}, \tag{5.3}$$

where the drag and inertia coefficients, $C_{D,\,\text{single}}$ and $C_{M,\,\text{single}}$, depend on the velocity amplitude U_{max} and period T. In addition, the relative importance of the drag and inertia forces depends on the Keulegan-Carpenter number, $N_{\text{KC}} = U_{max} T/\mathcal{D}$. It is known that inertia dominates if $N_{\text{KC}} < 5$ and drag force dominates if $N_{\text{KC}} > 25$ [35]. Using for estimates $T = 5$–$10\,\text{s}$, $U_{max} = 0.1\,\text{m/s}$, and $\mathcal{D} = 0.1\,\text{m}$, we get $N_{\text{KC}} = 5$–10, suggesting that the two forces can be comparable. Experimental information on wave induced forces on a large array of cylinders is unfortunately lacking. In the absence of similar information of dynamic waves forces on an array of cylinders, we propose a heuristic estimation of the eddy viscosity from an energy argument.

Consider a unit cell with height h, the local viscous dissipation rate is, in physical dimensions,

$$\mathcal{E} = \rho \nu_e \int_{-h}^{0} \iint_{\Omega_f} \left[\frac{1}{2} \left(\frac{\partial u_i}{\partial x_j} + \frac{\partial u_j}{\partial x_i} \right)^2 + \left(\frac{\partial u_i}{\partial z} + \frac{\partial w}{\partial x_i} \right)^2 + \left(\frac{\partial w}{\partial z} \right)^2 \right] d\Omega dz. \tag{5.4}$$

On the other hand, the rate of work done by the surface wave over the volume of a unit cell can be modeled by the macro quantity as

$$\mathcal{P} = \int_{-h}^{0} \left[\frac{1}{2} C_D U|U| \mathcal{D} + C_M \frac{\partial U}{\partial t} \frac{\pi \mathcal{D}^2}{4} \right] U \, dz, \tag{5.5}$$

if Morison's formula is assumed for the wave force per unit cell of a cylinder array, where $U = \langle u_1 \rangle$ is the cell-averaged horizontal velocity. Coefficients C_D and C_M, which can be functions of time, are to be determined empirically.

Since extensive experimental data for a large array of cylinders exist only for steady flows [4, e.g.,], we rest content with time-independent C_D and C_M. Therefore, a time-invariant eddy viscosity, $\nu_e = \nu_e(X_i)$, can be obtained from the energy balance argument by equating the time averages of $\mathcal{E}$ and $\mathcal{P}$,

$$\overline{\mathcal{E}} = \frac{1}{T} \int_{t}^{t+T} \mathcal{E} \, dt = \overline{\mathcal{P}} = \frac{1}{T} \int_{t}^{t+T} \mathcal{P} \, dt, \tag{5.6}$$

where the overbar denotes the average over a wave period T. A detailed derivation of equation stating the balance of mechanical energy over the volume of unit cell can be found in Mei et al. [19].

For the averaged dissipation rate, we shall use the computed $u_i^{(0)}$ and $w^{(0)}$ in the cell, based on the eddy viscosity in the last iteration[1] (as to be discussed in §7.2). Adopting only the leading order approximation, the time-averaged dissipation rate is

$$\begin{aligned}\overline{\mathcal{E}} &= \rho\nu_e \int_{-h}^{0} dz \iint_{\Omega_f} dx_1 dx_2 \left\{ 2\overline{\left[\left(\frac{\partial u_1^{(0)}}{\partial x_1}\right)^2 + \left(\frac{\partial u_2^{(0)}}{\partial x_2}\right)^2 + \epsilon^2\left(\frac{\partial w^{(0)}}{\partial z}\right)^2\right]} \right.\\ &\left. + \overline{\left(\frac{\partial u_1^{(0)}}{\partial x_2} + \frac{\partial u_2^{(0)}}{\partial x_1}\right)^2} + \overline{\left(\epsilon\frac{\partial u_1^{(0)}}{\partial z} + \frac{\partial w^{(0)}}{\partial x_1}\right)^2} + \overline{\left(\epsilon\frac{\partial u_2^{(0)}}{\partial z} + \frac{\partial w^{(0)}}{\partial x_2}\right)^2} \right\}\\ &= \rho\nu_e \int_{-h}^{0} dz \iint_{\Omega_f} dx_1 dx_2 \left\{ 2\overline{\left[\left(\frac{\partial u_1^{(0)}}{\partial x_1}\right)^2 + \left(\frac{\partial u_2^{(0)}}{\partial x_2}\right)^2\right]} \right.\\ &\left. + \overline{\left(\frac{\partial u_1^{(0)}}{\partial x_2} + \frac{\partial u_2^{(0)}}{\partial x_1}\right)^2} + \overline{\left(\frac{\partial w^{(0)}}{\partial x_1}\right)^2} + \overline{\left(\frac{\partial w^{(0)}}{\partial x_2}\right)^2} \right\} + \mathcal{O}(\epsilon),\end{aligned}$$

i.e.,

$$\overline{\mathcal{E}} = \rho\nu_e \int_{-h}^{0} dz \iint_{\Omega_f} \frac{1}{2}\overline{\left(\frac{\partial u_i^{(0)}}{\partial x_j} + \frac{\partial u_j^{(0)}}{\partial x_i}\right)^2 + \left(\frac{\partial w^{(0)}}{\partial x_i}\right)^2} d\Omega. \tag{5.7}$$

Regarding the averaged rate of work done by the wave force, the inertia term has no contribution due to time periodicity. Hence, $\overline{\mathcal{P}}$ depends only on the averaged drag:

$$\overline{\mathcal{P}} = \frac{1}{2}\rho\mathcal{D}C_D \int_{-h}^{0} \overline{\langle u_1^{(0)}\rangle^2 \left|\langle u_1^{(0)}\rangle\right|} dz + \mathcal{O}(\epsilon). \tag{5.8}$$

Recently, Cheng and Nguyen [4] have collected from various sources comprehensive data on the drag force on a cylinder array in a steady flow for a wide range of flow conditions and vegetation density. In terms of the Reynolds number Re_v defined by the depth-averaged velocity U_{ave} and the hydraulic radius r_v which incorporates the vegetation density (or porosity n), all data in the range of $52 < \mathrm{Re}_v < 5.6 \times 10^5$ fall tightly on the empirical curve

$$C_{D,\,\mathrm{steady}} = \frac{50}{\mathrm{Re}_v^{0.43}} + 0.7\left[1 - \exp\left(-\frac{\mathrm{Re}_v}{15{,}000}\right)\right], \tag{5.9}$$

where

$$\mathrm{Re}_v = \frac{U_{ave} r_v}{\nu}, \quad r_v = \frac{\pi\mathcal{D}}{4}\frac{n}{1-n}. \tag{5.10}$$

[1] Thanks to suggestions by Drs. Benlong Wang and Xiaoyu Guo of Shanghai Jiao Tong University, China.

and r_v is the hydraulic radius. Since we are not aware of any empirical formula for transient flow through a cylinder array, we assume the time-independent drag coefficient in (5.8) to be

$$C_D = \alpha C_{D,\,\text{steady}}, \tag{5.11}$$

where $C_{D,\,\text{steady}}$ is given by (5.9) and $\alpha = \mathcal{O}(1)$ is a fitting parameter to account for the possible difference between static and dynamic wave force coefficients. This choice amounts to assuming that C_D and $C_{D,\,\text{steady}}$ have similar dependence on the flow rate and the porosity.

In calculating the Reynolds number Re_v, the dimensional time-averaged horizontal velocity is given by

$$U_{ave} = \omega a_0 \frac{2}{\pi}\frac{1}{h}\int_{-h}^{0}\left|-\langle\widetilde{K}_{11}\rangle\frac{\partial\widetilde{p}^{(0)}}{\partial X}\right|dZ, \tag{5.12}$$

Recall (3.18) and (4.1), an eddy viscosity for two-dimensional waves can then be obtained from (5.6) as

$$\frac{\nu_e(X)}{\omega a_0 \mathcal{D}} = \frac{\frac{2}{3\pi}C_D\left|\langle\widetilde{K}_{11}\rangle\right|^3\int_{-h}^{0}\left|\frac{\partial\widetilde{p}^{(0)}}{\partial X}\right|^3 dZ}{\mathcal{F}_K\int_{-h}^{0}\left|\frac{\partial\widetilde{p}^{(0)}}{\partial X}\right|^2 dZ + \mathcal{F}_W\int_{-h}^{0}\left|\frac{\partial\widetilde{p}^{(0)}}{\partial Z}\right|^2 dZ}, \tag{5.13}$$

where

$$\mathcal{F}_K = \iint_{\Omega_f}\left\{\left|\frac{\partial\widetilde{K}_{11}}{\partial x_1}\right|^2 + \left|\frac{\partial\widetilde{K}_{21}}{\partial x_2}\right|^2 + \frac{1}{2}\left(\left|\frac{\partial\widetilde{K}_{11}}{\partial x_2}\right|^2 + \left|\frac{\partial\widetilde{K}_{21}}{\partial x_1}\right|^2\right) + \Re\left[\frac{\partial\widetilde{K}_{11}^*}{\partial x_2}\frac{\partial\widetilde{K}_{21}}{\partial x_1}\right]\right\}d\Omega, \tag{5.14}$$

$$\mathcal{F}_W = \iint_{\Omega_f}\frac{1}{2}\left(\left|\frac{\partial\widetilde{W}}{\partial x_1}\right|^2 + \left|\frac{\partial\widetilde{W}}{\partial x_2}\right|^2\right)d\Omega, \tag{5.15}$$

in dimensionless variables and $\widetilde{K}_{11}^*$ denotes the complex conjugate of $\widetilde{K}_{11}$. We stress that the eddy viscosity depends only on the macro-scale coordinate X and must be computed from the pressure amplitude $\widetilde{p}^{(0)}(X, Z)$ from the previous iteration. Finally, if experimental data on the transient force on a cylinder array become available, the present scheme can be modified by adding a time-dependent correction, $\nu_e^{corr}(t)$, to the time-averaged part in (5.13).

We now turn to the macro-scale problem and the iteration procedure for eddy viscosity.

6 Macro-scale equations in the forest

Substituting (3.18) into the equation of continuity, (3.5), and averaging over the unit cell, we obtain

$$\frac{\partial\langle\widetilde{u}_i^0\rangle}{\partial X_i} + \frac{\partial\langle\widetilde{w}^0\rangle}{\partial Z} = 0, \tag{6.1}$$

where Gauss's theorem, Ω-periodicity, and the no-slip conditions on S_B have been employed.

Similarly, by taking the cell average of (3.8) and (3.10) and using Gauss's theorem, we obtain

$$-\mathrm{i}\langle\widetilde{u}_i^{(0)}\rangle = -n\frac{\partial\widetilde{p}^{(0)}}{\partial X_i} - \frac{1}{\Omega}\left[\iint\limits_{\Omega_f}\left(-\frac{\partial\widetilde{A}_k}{\partial x_i} + \sigma\frac{\partial^2 K_{ik}}{\partial x_j\partial x_j}\right)d\Omega\right]\frac{\partial\widetilde{p}^0}{\partial X_k}$$

$$= -n\frac{\partial\widetilde{p}^{(0)}}{\partial X_i} - \frac{1}{\Omega}\left[\oint\limits_{S_B}\left(-\widetilde{A}_k\delta_{ij} + \widetilde{\tau}_{ij}^{(k)}\right)n_j^{S_B}ds\right]\frac{\partial\widetilde{p}^{(0)}}{\partial X_k} \tag{6.2}$$

and

$$-\mathrm{i}\langle\widetilde{w}^{(0)}\rangle = -n\frac{\partial\widetilde{p}^{(0)}}{\partial Z} - \frac{1}{\Omega}\left[\iint\limits_{\Omega_f}\sigma\frac{\partial^2\widetilde{W}}{\partial x_j\partial x_j}d\Omega\right]\frac{\partial\widetilde{p}^{(0)}}{\partial Z},$$

$$= -n\frac{\partial\widetilde{p}^{(0)}}{\partial Z} - \frac{1}{\Omega}\left[\oint\limits_{S_B}\sigma\frac{\partial\widetilde{W}}{\partial x_j}n_j^{S_B}\,ds\right]\frac{\partial\widetilde{p}^{(0)}}{\partial Z}, \tag{6.3}$$

where $n_j^{S_B}$ is the unit normal to the cylinder wall S_B.

Equations (6.1)–(6.3) are the effective equations governing $\langle\widetilde{u}_i^{(0)}\rangle$, $\langle\widetilde{w}^{(0)}\rangle$, and $\widetilde{p}^{(0)}$ in the wave motion on the macro scale. We point out that $\widetilde{p}^{(0)} = \langle\widetilde{p}^{(0)}\rangle$ is its own cell average because of (3.16). Physically, the line integrals in (6.2) and (6.3) represent the horizontal and vertical forces on the cylinder surface in the cell due to unit pressure gradient in waves.

Let us define the complex coefficients,

$$M_{ik} = \frac{1}{\Omega}\iint\limits_{\Omega_f}\left(-\frac{\partial\widetilde{A}_k}{\partial x_j} + \sigma\frac{\partial^2\widetilde{K}_{ik}}{\partial x_j\partial x_j}\right)d\Omega = -\mathrm{i}\delta_{\mathrm{ik}} - \mathrm{i}\langle\mathrm{K_{ik}}\rangle, \tag{6.4}$$

and

$$N = \frac{1}{\Omega}\iint\limits_{\Omega_f}\sigma\frac{\partial^2\widetilde{W}}{\partial x_j x_j}d\Omega = -n - \mathrm{i}\langle\mathrm{W}\rangle, \tag{6.5}$$

where (4.3) and (4.9) have been used. Equations (6.2) and (6.3) are rewritten as

$$-\mathrm{i}\langle\widetilde{u}_i^{(0)}\rangle = -n\frac{\partial\widetilde{p}^{(0)}}{\partial X_i} - M_{ik}\frac{\partial\widetilde{p}^{(0)}}{\partial X_k} \tag{6.6}$$

and

$$-\mathrm{i}\langle\widetilde{w}^{(0)}\rangle = -(n+N)\frac{\partial\widetilde{p}^{(0)}}{\partial Z}, \tag{6.7}$$

respectively. It is convenient to define a complex potential $\phi(X_i, Z)$ by

$$\widetilde{p}^{(0)} = \mathrm{i}\phi, \tag{6.8}$$

so that

$$\langle\widetilde{u}_i^{(0)}\rangle = n\frac{\partial\phi}{\partial X_i} + M_{ik}\frac{\partial\phi}{\partial X_k}, \quad \langle\widetilde{w}^{(0)}\rangle = (n+N)\frac{\partial\phi}{\partial Z}. \tag{6.9}$$

In terms of these the continuity equation, (6.1), is transformed to

$$\frac{\partial}{\partial X_k}\left[(n+M_{ik})\frac{\partial \phi}{\partial X_i}\right]+(n+N)\frac{\partial^2\phi}{\partial Z^2}=0,\quad i,k=1,2. \tag{6.10}$$

From (3.12) and (3.13), we obtain the dynamic and kinematic conditions on the free surface at the leading order:

$$\widetilde{\zeta}^{(0)}=\widetilde{\zeta}^{(0)}(X_i)=\widetilde{p}^{(0)}(X_i,0), \tag{6.11}$$

$$\langle\widetilde{w}^{(0)}\rangle=-\mathrm{i}n\widetilde{p}^{(0)},\quad Z=0. \tag{6.12}$$

On the sea bed, we have from (3.11)

$$\langle\widetilde{w}^{(0)}\rangle=0,\quad Z=-h. \tag{6.13}$$

In terms of the potential ϕ, they become

$$\widetilde{\zeta}^{0}(X_i)=\mathrm{i}\phi(X_i,0), \tag{6.14}$$

$$\frac{\partial\phi}{\partial Z}-\frac{n}{n+N}\phi=0,\quad Z=0, \tag{6.15}$$

$$\frac{\partial\phi}{\partial Z}=0,\quad Z=-h. \tag{6.16}$$

In general, M_{ik} and N are complex functions of $\vec{X}$ and of ω, and are to be evaluated from the solutions of the cell problems. The linear macro-scale problem for the complex potential ϕ must be solved numerically. In the absence of vegetation, i.e., $n=1$ and $M_{ik}=N=0$, (6.10)–(6.16) reduce to the familiar equations for linear water waves. For simple cells illustrated in Figs. 1 and 3, symmetry of K_{ik} dictates from (6.4) that $M_{11}=M_{22}\equiv M$ and $M_{12}=M_{21}=0$.

Later we shall consider wave propagation through a forest of cylinders of large but finite extent. In open water without the vegetation, $n=1$ and $M_{jk}=N=0$ we have

$$u_i=\frac{\partial\phi}{\partial X_i},\quad w=\frac{\partial\phi}{\partial Z} \tag{6.17}$$

while the potential satisfies Laplace's equation

$$\frac{\partial^2\phi}{\partial X_i\partial X_i}+\frac{\partial^2\phi}{\partial Z^2}=0 \tag{6.18}$$

and the boundary conditions

$$\frac{\partial\phi}{\partial Z}-\phi=0,\quad Z=0, \tag{6.19}$$

$$\frac{\partial\phi}{\partial Z}=0,\quad z=-h. \tag{6.20}$$

7 Two-dimensional scattering by a finite forest belt

Since relevant experimental data has only been found for unidirectional waves in a wave flume, we shall limit our attention to the two-dimensional problem in the vertical plane, i.e., the scattering of a plane wave normally incident on a forest belt in the finite region

$0 < X < L_B$, where L_B is the thickness of the forest. The belt is infinitely long in the transverse Y direction.

7.1 Numerical solution of the forest problem at one stage of iteration

We shall divide the domain into three regions: incidence zone (I), $X < 0$; the forest (F), $0 < X < L_B$; and transmission zone (T), $X > L_B$. The formal solutions in incidence and transmission zones where $n = 1$ and $M_{ik} = N = 0$ are known to be

$$\phi^{\mathrm{I}}(X, Z) = A_0 e^{\mathrm{i}k_0 X} \frac{\cosh k_0(Z+h)}{\cosh k_0 h} + \sum_{p=0}^{\infty} B_p e^{-\mathrm{i}k_p X} \frac{\cosh k_p(Z+h)}{\cosh k_p h} \tag{7.1}$$

and

$$\phi^{\mathrm{T}}(X, Z) = \sum_{p=0}^{\infty} E_p e^{\mathrm{i}k_p X} \frac{\cosh k_p(Z+h)}{\cosh k_p h}, \tag{7.2}$$

respectively, where k_p satisfies the well-known dispersion relationship

$$1 = k_p \tanh k_p h. \tag{7.3}$$

Note that k_0 is real and k_p, $p = 1, 2, 3, \ldots$ are imaginary roots. From the given incident wave profile, coefficient A_0 can be obtained from (6.14)

$$A_0 = -\mathrm{i}. \tag{7.4}$$

$B_0 = A_0 R$ and $E_0 = A_0 T$ are proportional to the reflection ($|R|$) and transmission ($|T|$) coefficients, respectively.

Inside the forest, $\phi^{\mathrm{F}}(X, Z)$ is governed by (6.10) with $M_{ik} = M(X)\delta_{ik}$, i.e.,

$$\frac{\partial}{\partial X}\left[(n+M)\frac{\partial \phi^{\mathrm{F}}}{\partial X}\right] + (n+N)\frac{\partial^2 \phi^{\mathrm{F}}}{\partial Z^2} = 0, \tag{7.5}$$

subject to the boundary conditions (6.15) and (6.16), and continuity of pressure and flux with the open water potentials outside the forest. Numerical solution of these equations is found by three-point second-order finite differences, and matched with the velocity potentials in open waters outside. Requiring continuity of pressure and horizontal velocity at discrete points on the interfaces at $X = 0$ and $X = L_B$ leads to a matrix equation for the discrete unknown inside and expansion coefficients outside the forest. The matrix equation is solved numerically.

For constant M and N, the forest problem is similar to that for the classical scattering problem in an open sea of constant depth [20]. In order to confirm our numerical scheme, the series solution in incidence and transmission zones and analytical solution inside the forest are presented in Appendix. The analytical solution has been used to verify the correctness of our finite difference solutions.

7.2 Numerical procedure of iteration for eddy viscosity

We note from (5.13) that $\nu_e(X)$ needs to be computed at sufficient number of macro-stations, $0 = X_1 < X_2 < \cdots < X_{N_c} = L_B$. Using the wave pressure $p^{(0)}(X, Z)$ from the previous iteration, $\nu_e(X_n)$ are first calculated from (5.13) at N_c macro stations where the cell problems must be solved by finite elements. These micro-cell results are used to compute the coefficients

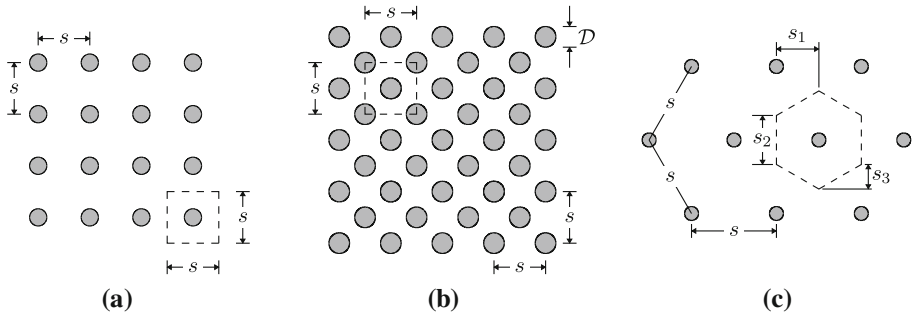

Fig. 3 Array configurations of three different laboratory forests. **a** NTU model employed by Mei et al. [21]. The cylinder diameter is $\mathcal{D} = 1$ cm, the spacing is $s = 3$ cm, and the cell porosity is $n = 0.913$. **b** Augustin [2]: $\mathcal{D} = 1.2$ cm, $s = 10.2$ cm, and $n = 0.978$. **c** Wu et al. [41] and Ozeren and Wren [42]: $\mathcal{D} = 0.94$ cm, $s = 5.74$ cm ($n = 0.976$) or $s = 4.31$ cm ($n = 0.957$). $s\_1 = 0.5s$, $s\_2 = s/\sqrt{3}$, and $s\_3 = s/2\sqrt{3}$. In each case, the unit cell is marked by the *dashed polygons*

$M(X_n)$ and $N(X_n)$ for the macro-scale problem of the wave field, which is then solved by finite differences for the next iteration. The calculation is repeated until convergence is achieved. Tests have shown that convergence can be achieved after less than ten iterations if the maximum relative error of v_e among all stations is less than 0.5 %.

8 Simulation of flume experiments

Three flume experiments with regular waves passing through periodic arrays of rigid and vertical cylinders have been reported in the literature. The experiments at Nangyang Technological University (NTU), Singapore were for a mixture of long and intermediate waves and have been simulated before for comparison with a long-wave theory [21], where the eddy viscosity was taken to be constant everywhere despite the spatial variation of the mean flow. Here we re-simulate the same tests by the present theory with a spatially varying eddy viscosity free of order-of-magnitude estimates. The experiments by Augustin [2], Wu et al. [41], and Ozeren and Wren [42] were all for intermediate wavelength comparable to the water depth hence provide a more comprehensive comparison. In our simulation the parameter α is chosen by fitting the wave amplitude record at one of the measuring stations, and predictions are then compared with records at all other stations. The lattice configurations in the three experiments are shown in Fig. 3.

8.1 NTU experiments

In the tests reported by Mei et al. [21] only the reflection coefficient, $|R|$, and transmission coefficient, $|T|$, of periodic waves were available. Figure 3a illustrates the lattice configuration of the 1.08 m thick forest, composed of perspex cylinders of 1 cm diameter. The water depth was constant at 12 cm while the wave period T varied from 0.8 to 3 s covering $kh \approx 1$–0.23 where k is the incident wavenumber. Hence most of the waves are rather long compared to depth. Other conditions and parameters are shown in Table 1. The recorded and predicted scattering coefficients $|T|$ and $|R|$ are shown in Fig. 4. In our calculations, the eddy viscosity is evaluated by (5.13) with the fitting parameter α, see (5.11), determined by best fit to the measured transmission coefficient (i.e., the wave displacement) at $X = L_B$. Values of α range from 1 to 3 (see Table 1). To test the sensitivity of α, we have performed additional

Table 1 Experimental conditions for periodic waves through a 1.08 m thick forest reported by Mei et al. [21]

Case	T (s)	A (cm)	λ (m)	kh	ka_0	α	Re_v	C_D	σ
T08	0.8	1.16	0.76	1.00	0.096	2.55	3,195	4.36	0.0034
T10	1.0	1.27	1.00	0.76	0.080	2.46	3,665	4.02	0.0055
T12	1.2	1.36	1.23	0.61	0.070	2.43	4,026	3.86	0.0081
T14	1.4	1.23	1.46	0.52	0.053	2.28	3,814	3.67	0.0089
T16	1.6	1.20	1.68	0.45	0.045	2.69	3,599	4.42	0.0128
T18	1.8	1.22	1.90	0.40	0.040	1.77	4,055	2.79	0.0096
T19	1.9	1.22	2.02	0.37	0.038	1.07	4,444	1.64	0.0055
T20	2.0	0.34	2.13	0.36	0.010	2.13	1,272	5.05	0.0050
T25	2.5	0.33	2.68	0.28	0.008	3.02	1,160	7.44	0.0106
T30	3.0	0.25	3.23	0.23	0.005	2.32	985	6.22	0.0080

T, a_0, and λ denote the wave period, wave amplitude, and wavelength of the tested waves, respectively. $k = 2\pi/\lambda$ is the wavenumber. In all cases, the water depth is fixed at $h = 12$ cm. Model coefficient α is obtained by the best fit of measured transmission coefficients (see Fig. 4). The Reynolds number Re_v, drag coefficient C_D, and dimensionless eddy viscosity σ are all functions of macro scale X as demonstrated in Fig. 5. Only their spatial averages within the forest are presented in this table to indicate their typical values

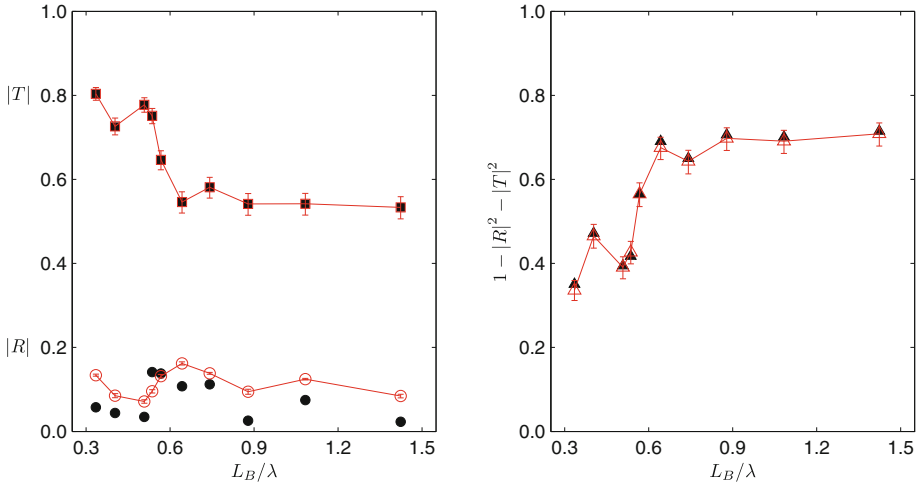

Fig. 4 Comparison of reflection coefficient, $|R|$, and transmission coefficient, $|T|$, for periodic waves through a 1.08 m thick model forest. $1-|R|^2-|T|^2$ measures the percentage of energy dissipation by the forest. *Solid marks* plot the measurements reported by Mei et al. [21]. Connected *hollow symbols* show the present theoretical predictions with *error bars* indicate the results of $\alpha(1 \pm 10\,\%)$. See Table 1 for the experimental conditions and Fig. 3a for the forest configuration

calculations using $\alpha(1 \pm 10\%)$, as illustrated in Fig. 4. The calculated reflection coefficient $|R|$ is shown to agree reasonably well with the experimental data. Overall, about 30–70 % of incident wave energy is dissipated by the model forest.

Figure 5 illustrates the spatial variation of the calculated dimensionless eddy viscosity, $\sigma(X)$, inside the forest. Values of σ decrease gradually in X, indicating attenuation of wave amplitude due to turbulence induced by wave-forest interactions. Undulations across the forest suggest the presence of incident (right-going) and reflected (left-going) waves. Sample variations of the coefficients M and N are shown for the shortest wave with $T = 0.8$ s (case

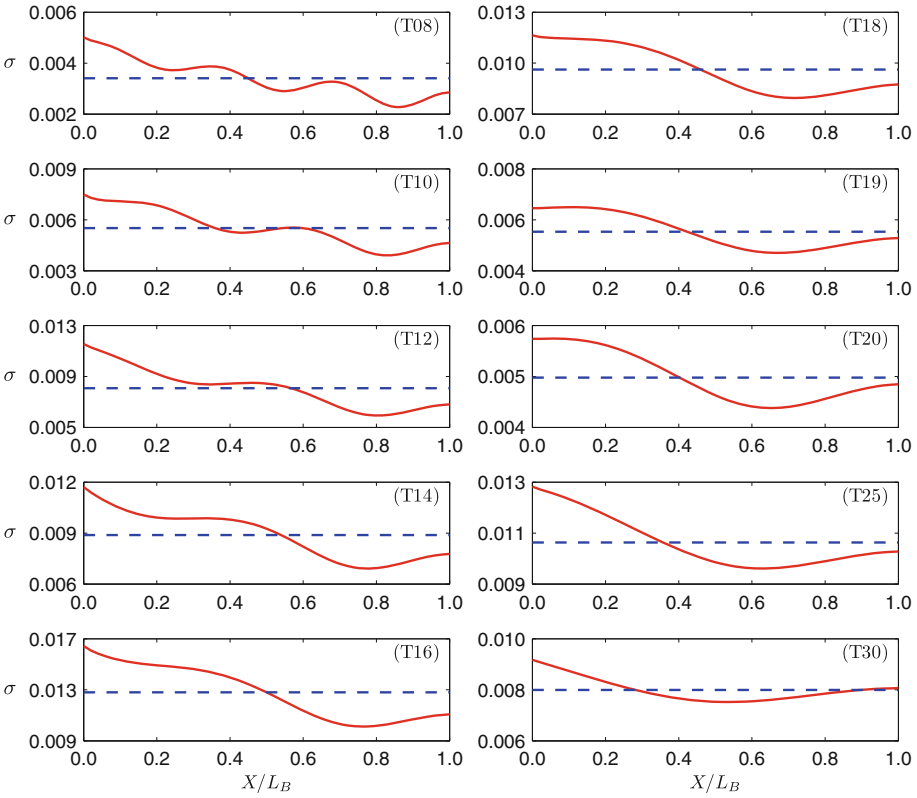

Fig. 5 Spatial variation of the calculated dimensionless eddy viscosity, $\sigma(X)$, inside the model forest. *Dashed lines* indicate the corresponding mean values, as listed in Table 1

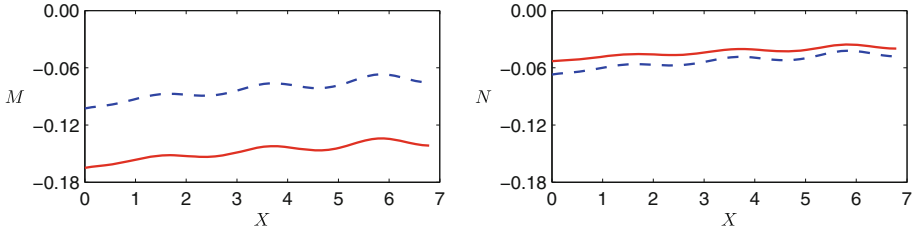

Fig. 6 Sample variation of the calculated complex coefficients, $M(X)$ and $N(X)$, inside the model forest for the case T08 listed in Table 1. *Solid* and *dashed lines* plot the real and imaginary parts, respectively

T08 in Table 4) in Fig. 6. Again some undulations across the forest appear due to the presence of partial standing waves. In Fig. 7 we plot both the dimensionless wave amplitude, $|\zeta(X)|$, and normalized $\sigma(X)$ across the forest for the case T08. Amplitude attenuation by the forest is evident.

In addition to the macro-scale predictions, our theory also provides Reynolds-averaged flow field in cells, which is needed in the study of transport and diffusion of solvents and nutrients in vegetated waters. Using again the short wave case T08 for demonstration, Fig. 8 illustrates the snapshots of velocity field around the cylinder in the middle of the forest ($X = 0.5L_B$) at dimensionless time $t/T = 0.31$ when the averaged velocity is near its maximum.

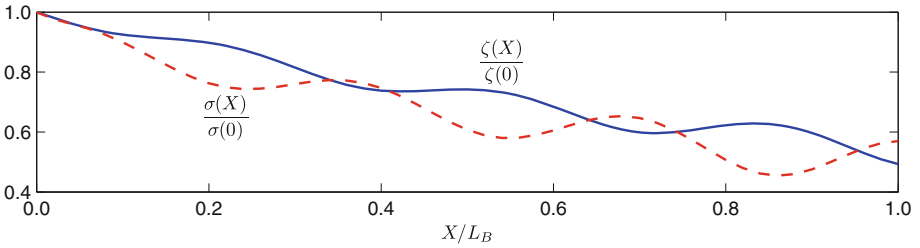

Fig. 7 Dimensionless wave amplitude, $|\zeta|$ (*solid line*), and, eddy viscosity, σ (*dashed line*), across the forest. Results correspond to the case T08 listed in Table 1

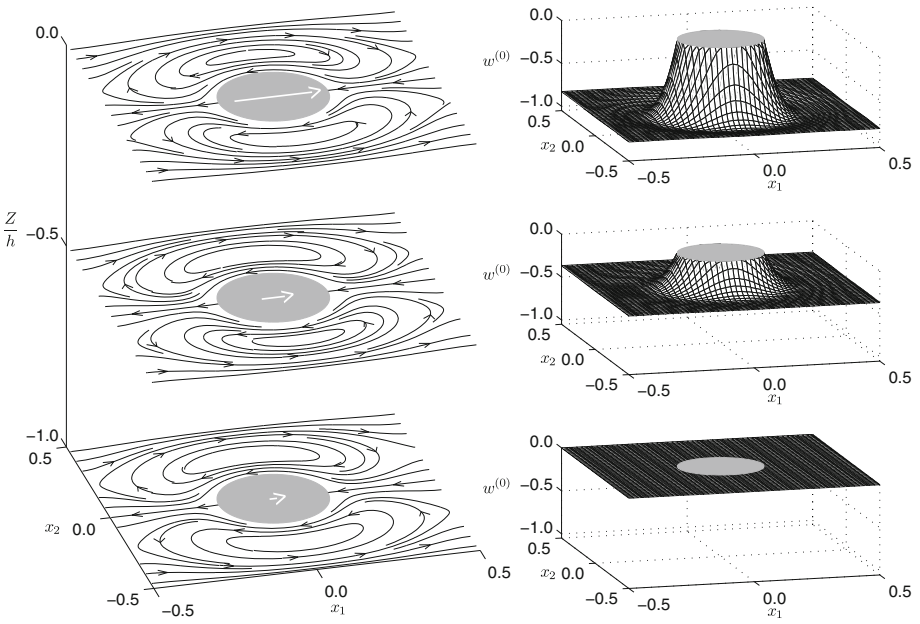

Fig. 8 Instantaneous velocity field around the cylinder sitting in the middle of the forest ($X = 0.5L_B$) at dimensionless time $t/T = 0.31$ for the case T08. *Left column* plots the projections of streamlines on three horizontal planes at $Z/h = 0, -0.5, -1$, respectively. *Arrows* denote the directions of micro velocity, $u_i^{(0)}$. *White vectors* at the *center* of the cylinder indicate the directions and relative magnitudes of the cell-averaged horizontal velocity, $\langle u^{(0)} \rangle$, at different levels. *Mesh plots* on the *right* show the distributions of the corresponding vertical velocity component, $w^{(0)}$. The origin of the micro coordinates, x_i, is set at the center of the unit cell

Projections of instantaneous streamlines at several depths $Z/h = 0, -0.5, -1$ as well as the distributions of vertical velocity component, $w^{(0)}$, inside this particular cell are shown. The streamlines are computed by MATLAB function *streamline* with linear interpolation from our velocity predictions at finite element nodes. As can be seen in Fig. 8, the density of streamlines hence the horizontal velocity decreases with depth while the flow patterns are similar at all depths. Furthermore, the vertical velocity $w^{(0)}$ (downward at this instant) is quite uniform horizontally away from the cylinder, but drops to zero rapidly near the cylinder. The flow reverses its direction after every half period. Figure 9 shows the horizontal flow patterns on the free surface at various instants within a half period, also in a cell at $X = 0.5L_B$. At

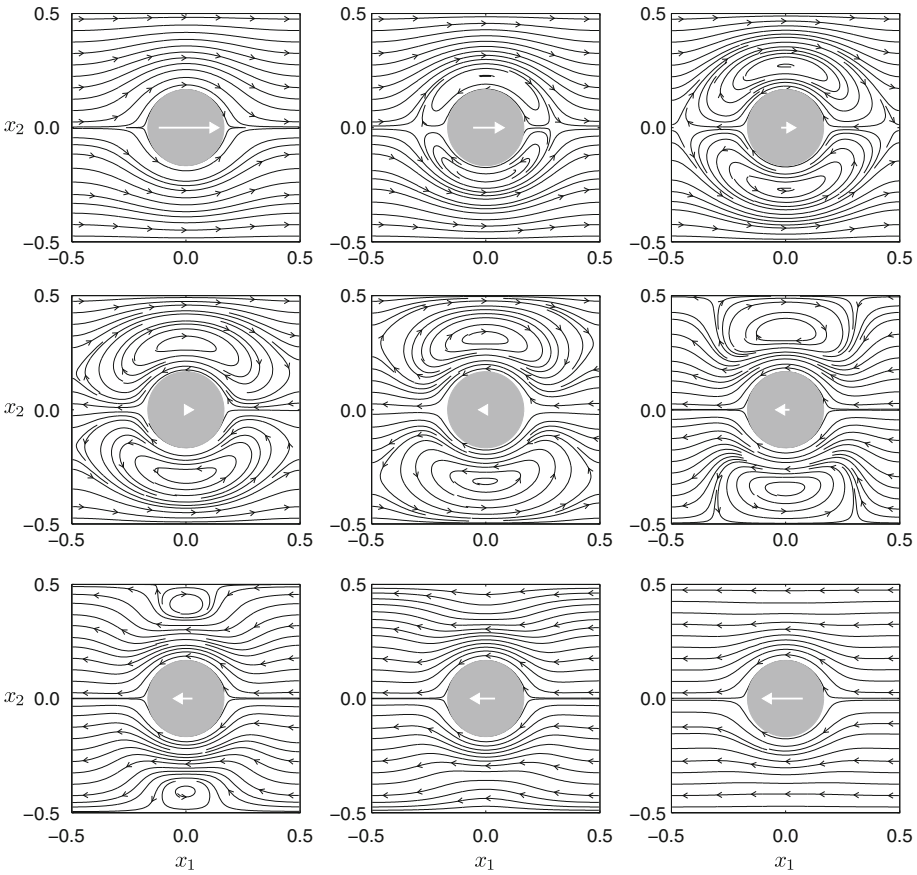

Fig. 9 Snapshots of free-surface streamlines in the middle of the forest for the case T08. From *left to right* and *top to bottom*, the dimensionless time is $t/T = 0.21, 0.27, 0.3, 0.31, 0.32, 0.33, 0.34, 0.35, 0.38$. *Arrows* indicate the flow directions while the *white vectors* at the *center* show the directions and relative magnitudes of $\langle u^{(0)} \rangle$

$t/T = 0.21$, when the averaged velocity (seepage velocity) is almost the greatest and the averaged acceleration the smallest in magnitude, a creeping flow is seen. As time increases, the surrounding flow slows down but the acceleration increases in magnitude. Symmetric eddies begin near the cylinder due to the boundary effect, and then move away towards the cell boundaries with diminishing intensity. This is followed by flow reversal and cyclic repetitions.

We stress that turbulent fluctuations are masked in the predictions here which represent only Reynolds' averages.

8.2 Experiments by Augustin [2]

The wave-vegetation experiments conducted by Augustin [2] are used here to further test our theory. Part of the data has been used by Augustin et al. [3] to calibrate the friction factor for a numerical model based on the Boussinesq-type equations for long waves.

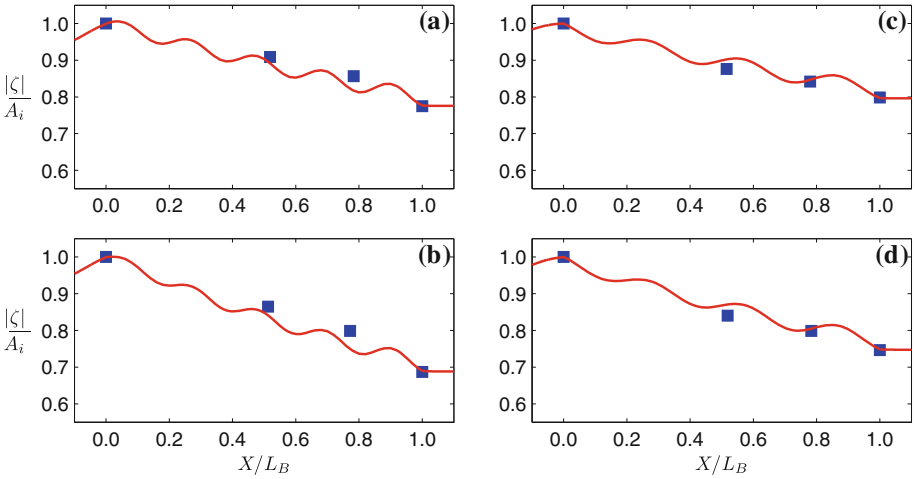

Fig. 10 Spatial variation of normalized wave amplitude, $|\zeta|/a_i$. *Line* present theoretical predictions. *Symbol* laboratory measurements by Augustin [2]. The forest has a thickness of 6 m and a porosity $n = 0.978$. The cell configuration is illustrated in Fig. 3b. Water depth is fixed at $h = 0.4$ m. Wave period, T, and wave amplitude measured at the entrance of the forest, a_i, are: **a** $T = 1.5$ s, $a_i = 4.5$ cm; **b** $T = 1.5$ s, $a_i = 6$ cm; **c** $T = 2$ s, $a_i = 5$ cm; **d** $T = 2$ s, $a_i = 6.5$ cm

In the experiments, the thickness of the model forest was 6 m. The lattice configuration is shown in Fig. 3b. The cylinder (wooden dowels) diameter and tree spacing were 1.2 and 10.2 cm, respectively. This corresponds to a forest porosity of $n = 0.978$. The free-surface elevation was recorded by five wave gauges spaced equally between two ends of the forest. However, records at the second gauge were not reported. Figure 10 compares our predictions with the measured amplitudes for four different cases (two water depths; two wave periods). The corresponding experimental conditions and parameters are listed in Table 2. Note that $kh = 0.98$ hence the waves are not long compared to depth. Again, in all calculations, the eddy viscosity was computed by (5.13) with values of α obtained by fitting the predictions to the measured amplitudes at the last station. As illustrated in Fig. 10, the quantitative agreement between theory and data at stations inside the forest is acceptable. We note that the values of macro Reynolds number (Re_v) and micro Reynolds number ($1/\sigma$) are all significantly greater than those of Mei et al. [21] (see Table 1). In addition, Re_v is close to the maximum in the experimental data range of Cheng and Nguyen [4] corresponding to the empirical formula of (5.9), $\mathrm{Re}_v \approx 5 \times 10^5$. Figure 10 shows that as much as 30 % amplitude reduction can occur as waves propagate through this forest as thick as two wavelengths.

8.3 Experiments of Wu et al. [41] and Wu et al. [42]

Wu and his colleagues (see e.g.,[41,42]) used birch dowels of 0.94 cm diameter to model emergent vegetation. The thickness of the laboratory forest was fixed at $L_B = 3.6$ m, whereas the porosity was either $n = 0.976$ or $n = 0.957$. Figure 3c illustrates the lattice pattern of the cylinder array. We use a regular hexagon to model a unit cell, similar to Zhong et al. [43] modeling blood flow in an alveolar sheet of lungs. Table 3 documents the experimental conditions of selected laboratory tests reported by Wu et al. [41] and [42]. The corresponding kh values ranged roughly from 1 to 4 representing a wide range of short incident waves. Drag coefficients evaluated by (5.11) are also listed in the same table.

Table 2 Experimental conditions of Augustin [2]

Case	T (s)	a_i (cm)	λ (m)	kh	ka_i	α	Re_v	C_D	σ
a	1.5	4.5	2.62	0.96	0.108	1.36	45,948	1.58	0.0004
b	1.5	6.0	2.62	0.96	0.144	1.71	57,517	1.94	0.0009
c	2.0	5.0	3.70	0.68	0.085	1.05	55,233	1.20	0.0006
d	2.0	6.5	3.70	0.68	0.111	1.14	69,490	1.26	0.0010

Water depth is fixed at $h = 0.4\,\mathrm{m}$. The forest has a thickness of $L_B = 6\,\mathrm{m}$ and a porosity of $n = 0.978$. a_i is the measured wave amplitude at the entrance of the forest. Re_v, C_D, and σ are the average values within the forest

Table 3 Laboratory experiments conducted by Wu and his colleagues

Case	T (s)	a_i (cm)	λ (m)	kh	ka_i	α	Re_v	C_D	σ
J1	0.7	2.65	0.77	4.11	0.218	2.35	7,263	3.23	0.0008
J2	1.0	5.00	1.51	2.08	0.208	2.26	20,333	2.76	0.0025
J3	0.7	2.65	0.77	4.11	0.218	2.02	3,332	3.45	0.0011
J4	1.0	5.00	1.51	2.08	0.208	2.56	8,912	3.41	0.0037
S1	1.0	1.90	1.46	1.72	0.082	2.55	10,733	3.28	0.0010
S2	1.2	3.90	1.94	1.30	0.127	2.95	21,301	3.60	0.0043
S3	1.4	3.05	2.39	1.05	0.080	3.40	18,248	4.18	0.0054
S4	1.0	3.10	1.51	2.08	0.129	2.43	13,687	3.05	0.0015
S5	1.2	4.25	2.05	1.53	0.130	2.73	20,310	3.34	0.0036
S6	1.4	3.40	2.57	1.22	0.083	3.84	17,325	4.73	0.0058

J1–J4: Wu et al. [42]. S1–S6: Wu et al. [41]. Water depth: $h = 0.5$ m for both J1–J4 and S4–S6; $h = 0.4\,\mathrm{m}$ in S1–S3. The forest thickness is fixed at $L_B = 3.66\,\mathrm{m}$. The porosity of the forest is either $n = 0.976$ (J1–J2, S1–S6) or $n = 0.957$ (J3, J4)

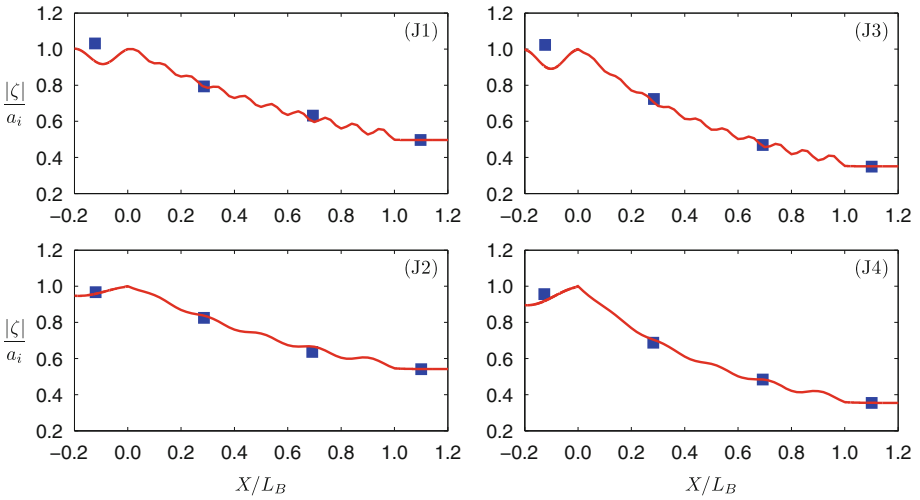

Fig. 11 Spatial variation of dimensionless wave amplitude, $|\zeta|/a_i$, inside the forest. *Symbols* show the laboratory data reported by Wu et al. [42]. *Solid lines* plot our theoretical predictions. The corresponding experimental conditions are listed in Table 3

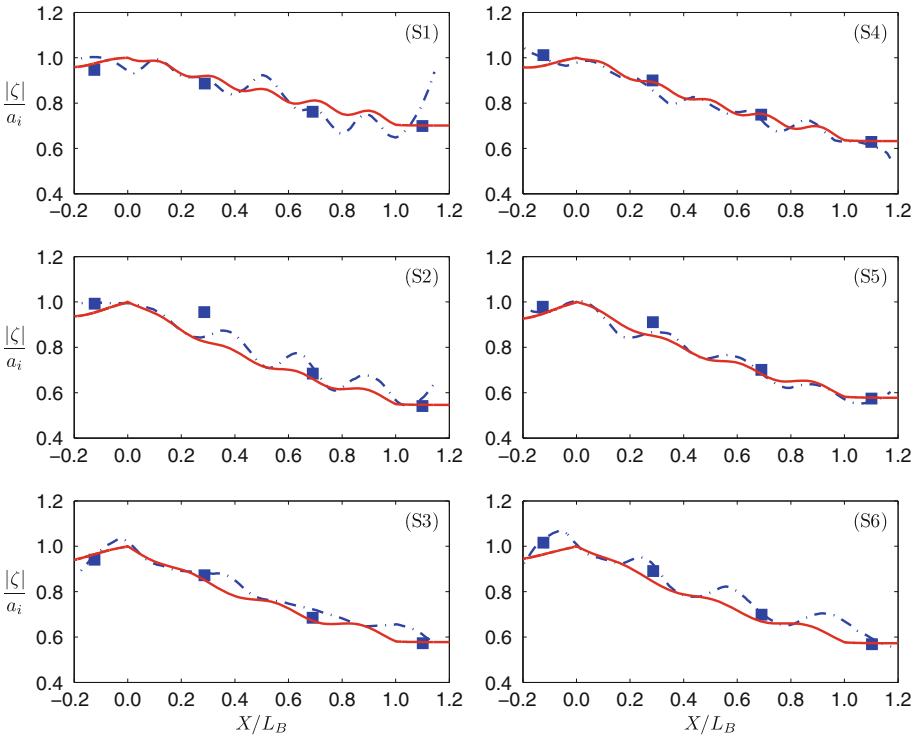

Fig. 12 Dimensionless wave amplitude, $|\zeta|/a_i$, inside the model forest. *Symbol* (gauge record) and *dashed-dotted line* (video imagery) are laboratory data derived by Wu et al. [41]. *Solid line*presents our predictions. See Table 3 for the experimental conditions

For all experiments, measurements of wave amplitude are available at four gauges across the forest. Wu et al. [41] also reported digital video images of wave amplitude distribution inside the forest for some cases. In Fig. 11 we compare the predictions of wave amplitude with gauge measurements for cases J1 to J4 listed in Table 3. In this set of experiments, $kh \approx 2, 4$ and $ka_i \approx 0.2$, where a_i is the measured amplitude at the entrance of the forest. The thickness of the forest, $L_B = 3.6$ m, is about 2.4–4.7 wavelengths of the incoming waves. Good agreements on the wave amplitude at gauge locations are evident for all four cases. The eddy viscosity was again calculated from (5.13) with parameter α obtained by fitting the measured data at the last station. Figure 12 compares the predictions of wave amplitude with laboratory data for cases S1–S6 listed in Table 3. The predicted partial standing wave pattern agrees qualitatively with the data derived from the videos. It should be mentioned that in the experiments reflection from the beach and re-reflection from the wavemaker were noticeable, as mentioned in Wu et al. [41]. Without more detailed records more precise simulation is hard to achieve.

9 Concluding remarks

The main objective of this study is to propose a micro-scale based, yet numerically expedient theory for modeling wave propagation through vegetated waters. For rigid and stationary

vertical cylinders in a periodic array, the sharp contrast of lattice spacing and wave length is exploited. By the use of homogenization technique (multiple scale perturbations), the micro-scale mechanics in a unit cell and the macro scale of waves are solved separately and not simultaneously. By reasoning that turbulence is primarily caused by the proximity of the cylinders, the eddy viscosity is calculated from an energy argument equating the averaged rate of dissipation to the work done by wave forces. Experimental data for forces on a cylinder array available only for a steady and uniform current is used. For simulating existing experiments, one fitting parameter appears to serve the purpose.

In existing numerical models of wave–vegetation interaction, the drag and inertia coefficients are obtained either by data fitting or using the values known for a single cylinder. It would be desirable to measure in the laboratory transient forces on a large array of vertical cylinders, so that the present theory can be extended to predict the time-dependent eddy viscosity. Transient eddy viscosity has been applied before for oscillatory boundary layers near the seabed by Trowbridge and Madsen [37], who treated cases where the transient part is a small perturbation.

One of the advantages of the homogenization method is that the micro-scale physics can be extracted after the macro-scale problem is solved, as shown by our sample predictions in a typical cell. This should enable the further development of a theory of convective diffusion which depends on the flow pattern in cells. It should be pointed out, however, that the homogenization theory is effective for linear or nearly linear problems only, hence for small amplitude waves. Under these restrictions, the method can be applied to elastic cylinders in waves as long as the deformation is also small. These extensions can be of interest to shoreline protection or to wave-induced spreading of pollutants or other solvents in vegetated waters, and will reported in the future.

Acknowledgments This work is supported by research grants from the National Science Foundation to Cornell University. CCM was also funded by a Mary Upson visiting professorship from Cornell University.

Appendix: A constant eddy viscosity model for wave scattering by a finite forest belt

For checking the numerical solution for variable M and N (see §7.1), we give the analytical solution for constant eddy viscosity.

The formal solutions in incidence zone and transmission zone are given by (7.2) and (7.3), respectively. For constant eddy viscosity in the forest region, M and N are complex constants. By separation of variables as for the open waters we obtain

$$\phi^{\mathrm{F}}(X, Z) = \sum_{q=0}^{\infty} \left[C_q \cos(\gamma \hat{k}_q x) + D_q \sin(\gamma \hat{k}_q x) \right] \frac{\cosh \hat{k}_q (Z + h)}{\cosh \hat{k}_q h}, \tag{A.1}$$

where $\gamma = \sqrt{(n + N)/(n + M)}$ and $\hat{k}_q$ are complex roots of the transcendental equation

$$1 = \left(1 + \frac{N}{n}\right) \hat{k}_q \tanh \hat{k}_q h. \tag{A.2}$$

Note that boundary conditions (6.14) and (6.15) have been used. C_q and D_q are coefficients to be determined.

Coefficients B_p, C_q, D_q, and E_p are to be determined by matching the pressure and the horizontal velocity component at the interfaces between two adjacent regions. At $X = 0$, the interfacial conditions are

$$\phi^{\mathrm{I}} = \phi^{\mathrm{F}}, \quad -h < Z < 0, \tag{A.3}$$

$$\frac{\partial \phi^{\mathrm{I}}}{\partial X} = (n+M)\frac{\partial \phi^{\mathrm{F}}}{\partial X}, \quad -h < Z < 0. \tag{A.4}$$

At $X = L_B$,

$$\phi^{\mathrm{F}} = \phi^{\mathrm{T}}, \quad -h < Z < 0, \tag{A.5}$$

$$(n+M)\frac{\partial \phi^{\mathrm{F}}}{\partial X} = \frac{\partial \phi^{\mathrm{T}}}{\partial X}, \quad -h < Z < 0. \tag{A.6}$$

The following condition of orthogonality applies to both k_p and $\hat{k}_q$:

$$\int_{-h}^{0} \cosh \kappa_m (Z+h) \cosh \kappa_n (Z+h) dZ = \begin{cases} 0, & m \neq n \\ \frac{2\kappa_m h + \sinh 2\kappa_m h}{4\kappa_m}, & m = n \end{cases}, \tag{A.7}$$

where $\kappa = k$ or $\hat{k}$. By truncating the series and using (A.7) in (A.3) and (A.6), we obtain

$$-\mathrm{i}\frac{\Gamma_{0q}}{\cosh k_0 h} + \sum_{p=0}^{P_r} B_p \frac{\Gamma_{pq}}{\cosh k_p h} = C_q \frac{\Pi\left(\hat{k}_q\right)}{\cosh \hat{k}_q h}, \quad q = 0, 1, 2, \ldots, Q, \tag{A.8}$$

$$\frac{k_0 \Pi\left(k_0\right)}{\cosh k_0 h}\delta_{0p} - \mathrm{i}B_p \frac{k_p \Pi\left(k_p\right)}{\cosh k_p h} = \gamma(n+M)\sum_{q=0}^{Q} D_q \frac{\hat{k}_q \Gamma_{pq}}{\cosh \hat{k}_q h}, \quad p = 0, 1, 2, \ldots, P_r, \tag{A.9}$$

at $X = 0$, and

$$\left[C_q \cos(\gamma \hat{k}_q L_B) + D_q \sin(\gamma \hat{k}_q L_B)\right] \frac{\Pi\left(\hat{k}_q\right)}{\cosh \hat{k}_q h} \tag{A.10}$$

$$= \sum_{p=0}^{P_t} E_p e^{\mathrm{i}k_p L_B} \frac{\Gamma_{pq}}{\cosh k_p h}, \quad q = 0, 1, 2, \ldots, Q,$$

$$\gamma(n+M)\sum_{q=0}^{Q}\left[-C_q \sin(\gamma \hat{k}_q L_B) + D_q \cos(\gamma \hat{k}_q L_B)\right] \frac{\hat{k}_q \Gamma_{pq}}{\cosh \hat{k}_q h} \tag{A.11}$$

$$= \mathrm{i}E_p e^{\mathrm{i}k_p L_B} \frac{k_p \Pi\left(k_p\right)}{\cosh k_p h}, \quad p = 0, 1, 2, \ldots, P_t,$$

at $X = L_B$, where

$$\Gamma_{pq} = \int_{-h}^{0} \cosh k_p (Z+h) \cosh \hat{k}_q (Z+h) dZ \tag{A.12}$$

$$= \frac{k_p \sinh k_p h \cosh \hat{k}_q h - \hat{k}_q \cosh k_p h \sinh \hat{k}_q h}{k_p^2 - \hat{k}_q^2},$$

$$\Pi(\kappa) = \frac{2\kappa h + \sinh 2\kappa h}{4\kappa}, \quad \kappa = k_p, \hat{k}_q. \tag{A.13}$$

In addition, P_r, Q, and, P_t are the finite terms after truncation in zones (I), (F), and (T), respectively. The expansion coefficients $\left(B_p, C_q, D_q, E_p\right)$ can now be obtained by solving numerically the above algebraic equations. Afterwards, $|R| = |B_0|$ and $|T| = |E_0|$ are the reflection and transmission coefficients respectively.

References

1. Asano T, Deguchi H, Kobayashi N (1992) Interactions between water waves and vegetation. Proc 23th Int Conf Coast Eng ASCE 3:2710–2723
2. Augustin LN (2007) Laboratory experiments and numerical modeling of wave attenuation through artificial vegetation. MS Thesis, Texas A&M University
3. Augustin LN, Irish JL, Lynett P (2009) Laboratory and numerical studies of wave damping by emergent and near-emergent wetland vegetation. Coast Eng 56:332–340
4. Cheng N-S, Nguyen HT (2011) Hydraulic radius for evaluating resistance induced by simulated emergent vegetation in open-channel flows. J Hydraul Eng 137:995–1004
5. Dalrymple RA, Kirby JT, Hwang PA (1984) Wave refraction due to areas of energy dissipation. J Waterw Port Coast Ocean Eng 110:67–79
6. Dubi A, Tørum A (1994) Wave damping by kelp vegetation. Proc 24th Int Conf Coast Eng ASCE 1:142–156
7. Fonsecaa MS, Cahalanb JA (1992) A preliminary evaluation of wave attenuation by four species of seagrass. Estuar Coast Shelf Sci 35:565–576
8. Harada K, Imamura F (2005) Effects of coastal forest on tsunami hazard mitigation—a preliminary investigation. In: Satake K (ed) Tsunamis: case studies and recent development. Advances in natural and technological hazards research, vol 23. Springer, Dordrecht, pp 279–292
9. Hiraishi T, Harada K (2003) Greenbelt tsunami prevention in south-Pacific region. Rep Port Airpt Res Inst 43:1–23
10. Huang Z, Yao Y, Sim SY, Yao Y (2011) Interaction of solitary waves with emergent rigid vegetation. Ocean Eng 38:1080–1088
11. Huang ZH, Zhang WB (2011) Wave attenuation through an array of rigid circular cylinders: a laboratory study. Asian Pac Coasts 2011:1826–1833
12. Kobayashi N, Raichlen AW, Asano T (1993) Wave attenuation by vegetation. J Waterw Port Coast Ocean Eng 199:30–48
13. Li CW, Yan K (2007) Numerical investigation of wave–current–vegetation interaction. J Hydraul Eng 133:794–803
14. Liu D, Diplas P, Fairbanks JD, Hodges CC (2008) An experimental study of flow through rigid vegetation. J Geophys Res 113:F04015. doi:10.1029/2008JF001042
15. Lowe RJ, Koseff JR, Monismith (2005) Oscillatory flow through submerged canopies: 1. Velocity structure. J Geophys Res 110:C10016. doi:10.1029/2004JC002788
16. Massel SR, Furukawa K, Brinkman RM (1999) Surface wave propagation in mangrove forests. Fluid Dyn Res 24:219–249
17. Mazda Y, Kobashi D, Okada S (2005) Tidal-scale hydrodynamics within mangrove swamps. Wetl Ecol Manag 13:647–655
18. Mazda Y, Wolanski E, King B, Sase A, Ohtsuka D, Magi M (1997) Drag force due to vegetation in mangrove swamps. Mangrove Salt Marsh 1:193–199
19. Mei CC, Stiassnie M, Yue DKP (2005) Theory and applications of ocean surface waves. Part I: Linear aspects. Eq. (9.2.16). World Scientific, Singapore, p 458
20. Mei CC, Black JL (1969) Scattering of surface waves by rectangular obstacles in waters of finite depth. J Fluid Mech 38:499–511
21. Mei CC, Chan I-C, Liu PL-F, Huang Z, Zhang W (2011) Long waves through emergent coastal vegetation. J Fluid Mech 461:461–491
22. Mendez FJ, Losada IJ (1999) Hydrodynamics induced by wind waves in a vegetation field. J Geophys Res 104:18383–18396. doi:10.1029/1999JC900119
23. Mendez FJ, Losada IJ (2004) An empirical model to estimate the propagation of random breaking and nonbreaking waves over vegetation fields. Coast Eng 51:103–118

24. Mo W (2010) Numerical investigation of solitary wave interaction with group of cylinders. Ph.D. Thesis, Cornell University
25. Morison JR, O'brien MP, Johnson JW, Schaaf SA (1950) The force exerted by surface waves on piles. Petrol Trans 189:149–154
26. Nepf HM (1999) Drag, turbulence, and diffusion in flow through emergent vegetation. Water Resour Res 35:479–489
27. Raupach MR, Shaw RH (1982) Averaging procedures for flow within vegetation canopies. Bound Layer Meteorol 22:79–90
28. Sarpkaya T, Isaacson M (1981) Mechanics of wave forces on offshore structures. Van Nostrand Reinhold, New York
29. Schutten J, Dainty J, Davy AJ (2004) Wave-induced hydraulic forces on submerged aquatic plants in shallow lakes. Ann Bot 93:333–341
30. Smagorinsky J (1963) General circulation experiments with the primitive equations. I. The basic experiment. Mon Weather Rev 91:99–164
31. Spalart PR, Allmaras SR (1994) A one-equation turbulence model for aerodynamic flows. La Recherche Aérospatiale 1:5–21
32. Stoesser T, Kim SJ, Diplas P (2010) Turbulent flow through idealized emergent vegetation. J Hydraul Eng 136:1003–1017
33. Stratigaki V, Manca E, Prinos P, Losada IJ, Lara JL, Sclavo M, Amos CL, Cáceres I, Sánchez-Arcilla A (2011) Large-scale experiments on wave propagation over Posidonia oceanica. J Hydraul Res 49:31–43
34. Strusińska-Correia A, Husrin S, Oumeraci H (2013) Tsunami damping by mangrove forest: a laboratory study using parameterized trees. Nat Hazards Earth Syst Sci 13:483–503
35. Sumer BM, Fredsøe J (2006) Hydrodynamics around cylindrical structures. World Scientific, Singapore
36. Tanino Y, Nepf HM (2008) Lateral dispersion in random cylinder arrays at high Reynolds number. J Fluid Mech 600:339–371
37. Trowbridge J, Madsen OS (1984) Turbulent boundary layers: 1. Model formulation and first-order solution; 2. Second-order theory and mass transport. J Geophys Res 89(7989–7997):7999–8007
38. Tschirky P, Hall K, Turcke D (2000) Wave attenuation by emergent wetland vegetation. Proc 27th Int Conf Coast Eng ASCE 3:865–877
39. Vo-Luong P, Massel S (2008) Energy dissipation in non-uniform mangrove forests of arbitrary depth. J Marine Syst 74:603–622
40. Wallace S, Cox R (2000) Effects of seagrass on nearshore current and wave dynamics. Proc 27th Int Conf Coast Eng ASCE 4:878–890
41. Wu W et al (2011) Investigation of surge and wave reduction by vegetation. SERRI Report 80037–01. U.S. Department of Homeland Security
42. Wu W, Zhang M, Ozeren Y, Wren D (2013) Analysis of vegetation effect on waves using a vertical 2D RANS model. J Coast Res 29:383–397
43. Zhong Z, Dai Y, Mei CC, Tong P (2002) A micromechanical theory of flow in pulmonary alveolar sheet. Comput Model Eng Sci 3:77–86